The Astrophysical Journal, 807:77 (13pp), 2015 July 1 doi:10.1088/0004-637X/807/1/77

GLOBAL STRUCTURE OF ISOTHERMAL DIFFUSE X-RAY EMISSION ALONG THE FERMI BUBBLES

J. Kataoka[1], M. Tahara[1], T. Totani[2], Y. Sofue[3], Y. Inoue[4], S. Nakashima[4], and C. C. Cheung[5]
[1] Research Institute for Science and Engineering, Waseda University, 3-4-1, Okubo, Shinjuku, Tokyo 169-8555, Japan; kataoka.jun@waseda.jp
[2] Department of Astronomy, The University of Tokyo, Bunkyo-ku, Tokyo 113-0033, Japan
[3] Institute of Astronomy, The University of Tokyo, Mitaka, Tokyo 181-0015, Japan
[4] Institute of Space and Astronautical Science, JAXA, 3-1-1 Yoshinodai, Chuo-ku, Sagamihara, Kanagawa 252-5210, Japan
[5] Space Science Division, Naval Research Laboratory, Washington, DC 20375, USA
Received 2015 January 29; accepted 2015 May 21; published 2015 July 1

ABSTRACT

In our previous works, we found absorbed thermal X-ray plasma with $kT \simeq 0.3$ keV observed ubiquitously near the edges of the Fermi bubbles and interpreted this emission as weakly shock-heated Galactic halo gas. Here we present a systematic and uniform analysis of archival *Suzaku* (29 pointings; 6 newly presented) and *Swift* (68 pointings; 49 newly presented) data within Galactic longitudes $|l| < 20°$ and latitude $5° \lesssim |b| < 60°$, covering the whole extent of the Fermi bubbles. We show that the plasma temperature is constant at $kT \simeq 0.30 \pm 0.07$ keV, while the emission measure (EM) varies by an order of magnitude, increasing toward the Galactic center (i.e., low $|b|$) with enhancements at the North Polar Spur (NPS), SE-claw, and NW-clump features. Moreover, the EM distribution of $kT \simeq 0.30$ keV plasma is highly asymmetric in the northern and southern bubbles. Although the association of the X-ray emission with the bubbles is not conclusive, we compare the observed EM properties with simple models assuming (i) a filled halo without bubbles, whose gas density follows a hydrostatic isothermal model (King profile), and (ii) a bubble-in-halo in which two identical bubbles expand into the halo, forming thick shells of swept halo gas. We argue that the EM profile in the north ($b > 0°$) favors (ii), whereas that of the south ($b < 0°$) is rather close to (i), but a weak excess signature is clearly detected also in the south like NPS (South Polar Spur). Such an asymmetry, if due to the bubbles, cannot be fully understood only by the inclination of bubbles' axis against the Galactic disk normal, thus suggesting asymmetric outflow due to different environmental/initial conditions.

Key words: Galaxy: center – Galaxy: halo – X-rays: ISM

1. INTRODUCTION

The "Fermi bubbles" are giant gamma-ray structures extending above and below the Galactic center (GC) for about 8 kpc (Dobler et al. 2010; Su et al. 2010; Ackermann et al. 2014). The gamma-ray emission of the bubbles is spatially correlated with the so-called *WMAP* haze, which is characterized by a spherical morphology with radius ~ 4 kpc centered at the GC, and was recently confirmed by *Planck* observations (Planck Collaboration et al. 2013). Moreover, the recently discovered giant linearly polarized radio lobes emanating from the GC also show a close correspondence to the Fermi bubbles (Carretti et al. 2013). It has thus been argued that the bubbles were created by some large episode of energy injection in the GC, such as an active galactic nucleus (AGN) like outburst (e.g., Guo et al. 2012; Yang et al. 2012) or from nuclear starburst activity (e.g., Lacki 2014) in the past with an energy release of 10^{55-56} erg over 10 Myr ago (Su et al. 2010; Crocker & Aharonian 2011; Carretti et al. 2013).

Interestingly, the idea of a nuclear outburst that happened in the GC was first proposed over 40 years ago, prior to the discovery of the Fermi bubbles (e.g., Sofue 1977, 1984, 1994, 2000; Bland-Hawthorn & Cohen 2003). Relatedly, a number of observations in X-rays have been discussed in the literature as evidence that the GC has experienced multiple epochs of enhanced source activity, including the Fe–K$_\alpha$ echo from molecular clouds (e.g., Koyama et al. 1996; Ryu et al. 2013) and the presence of an over-ionized clump with a jet-like structure (Nakashima et al. 2013). Particularly noteworthy is the giant Galactic feature called the North Polar Spur (NPS) that is seen in both X-ray and radio maps and believed to be a part of the radio Loop I structure. Sofue (2000) interpreted the NPS as a result of a large-scale outflow from the GC with a total energy of $\sim 10^{55-56}$ erg within a timescale of ~ 10 Myr, exactly consistent with the values discussed to create the Fermi bubbles above. In this context, Totani (2006) has shown that various other observational properties like the 511 keV line emission (e.g., Weidenspointner et al. 2008) in the GC can also be naturally explained in the framework of a radiatively inefficient accretion flow, if the outflow energy expected is 10^{56} erg or 3×10^{41} erg s^{-1}.

Assuming that the NPS and other prominent X-ray enhancements in the vicinity of the Fermi bubbles are all related in origin, we started a project consisting of X-ray observations along the edge regions of the Fermi bubbles since 2012, together with a systematic analysis of archival data provided by *Suzaku* and *Swift* over the past 10 yr. Kataoka et al. (2013, hereafter Paper I) first carried out 14 *Suzaku* X-ray observations positioned across the northeast and the southernmost edges of the Fermi bubbles with a total requested exposure of 280 ks. They found that the detected diffuse X-ray emission is reproduced by a three-component plasma model including unabsorbed thermal emission of the Local Bubble (LB: $kT \simeq 0.1$ keV), absorbed thermal emission related to the NPS and/or Galactic halo (GH: $kT \simeq 0.3$ keV), and a power-law component reproducing the cosmic X-ray background (CXB).

This finding was confirmed by Tahara et al. (2015, hereafter Paper II), who observed two other prominent X-ray structures, the north cap (N-cap) and southeast claw (SE-claw) seen in the *ROSAT* 0.75 keV image (Snowden et al. 1995) and/or MAXI all-sky survey mid-band image (1.7–4.0 keV; Kimura et al. 2013). Together with new evidence of a large amount of

neutral matter absorbing the thermal plasma, in Papers I and II we argued that the observed $kT \simeq 0.3$ keV gas was heated by a weak shock driven by the bubbles' expansion in the surrounding halo, with the corresponding velocity $v_{\rm exp} \sim 300\,{\rm km\,s^{-1}}$, which is consistent with the recent finding of a non-thermal velocity in the X-ray absorption line toward 3C 273 situated in the sightline of the Fermi bubbles (Fang & Jiang 2014; but see also Fox et al. 2015 for the ultraviolet absorption line features toward PDS 456). Such a low expansion velocity is also supported by some theoretical models discussing the Fermi bubbles' morphology (e.g., Crocker et al. 2014; Fujita et al. 2014; Mou et al. 2014). Also, Tahara et al. (2015) found possible evidence of 0.7 keV plasma in addition to 0.3 keV plasma in the northernmost region of the bubble.

While $kT \simeq 0.3$ keV plasma was ubiquitously observed in Papers I and II and was regarded as evidence of a shock-heated halo, these observations were highly biased toward the directions of X-ray enhancements and prominent structures like the NPS, N-cap, and SE-claw. In fact, given the large spatial extent of the Fermi bubbles within the Galactic longitudes $|l| < 20^\circ$ and latitudes $|b| < 60^\circ$, most of the bubbles' interior were unprobed. Thus, our goal in this paper is to determine the global characteristics and nature of diffuse X-ray emission associated with the Fermi bubbles, utilizing as many X-ray data pointings as possible. We thus analyzed a total of 29 archival data sets obtained with *Suzaku* (Mitsuda et al. 2007) and 68 archival data sets from *Swift* (Gehrels et al. 2004) whose pointing centers are situated at Galactic longitudes $|l| < 20^\circ$ and latitudes $5^\circ \lesssim |b| < 60^\circ$, spanning the full spatial extent of the Fermi bubbles above and below the GC. The observations and data reduction are described in Section 2. The analysis process and results for *Suzaku* and *Swift* are briefly summarized in Section 3. In Section 4, we discuss our findings in the context of proposed toy models assuming (i) a filled halo without bubbles and (ii) a bubble-in-halo geometry. We also discuss a possible origin of asymmetry in the Galactic latitude profiles of the derived X-ray EM observed in the north and south bubbles. Section 5 presents our conclusions.

2. OBSERVATIONS AND DATA REDUCTION

2.1. Suzaku XIS

As detailed in Papers I and II, we conducted dedicated *Suzaku* observations of the Fermi bubbles in 2012 and 2013 as a part of the AO7 and AO8 programs. The *Suzaku* satellite (Mitsuda et al. 2007) is equipped with four X-ray telescopes (XRTs; Serlemitsos et al. 2007), and each carries a focal-plane X-ray CCD camera (X-ray Imaging Spectrometer, XIS; Koyama et al. 2007a). One of the XIS sensors is a back-illuminated (BI) CCD (XIS1), and the other three are front-illuminated (FI) ones (XIS0, XIS2, and XIS3). The field of view of *Suzaku* XIS is $18' \times 18'$ with a telescope half-power diameter (HPD, i.e., the point-spread function) of $2'$. Since operation of XIS2 ceased in 2006 November owing to contamination by a leakage current, we use only three CCDs in this paper. Although *Suzaku* also carries a hard X-ray detector (Takahashi et al. 2007), we do not use the data collected by its PIN and GSO instruments because thermal emission we described above is too faint to be detected at above 10 keV and no statistically significant excess over the CXB was found with these PIN/GSO detectors. In the AO7 program (280 ks total; Paper I), eight pointings overlapped with the northeast bubble edge and across part of the NPS, with the remaining six pointings across the southernmost edges of the bubble. In AO8, we carried out four observations of 20 ks each, pointed "on" and "off" the (i) N-cap and (ii) SE-claw regions (2015).

For this paper, we further investigated archived *Suzaku* observations pointing toward the interior of the Fermi bubbles or in their close vicinity, covering $|l| < 20^\circ$ and $|b| < 60^\circ$. We selected pointings in which (i) the normal XIS observing mode was adopted throughout the observation, (ii) no bright X-ray features, such as compact sources and cluster gas, exist in the same filed of view that may affect the analysis of diffuse X-ray emission, and (iii) $|b| \gtrsim 5^\circ$ to avoid strong contamination from the GC region and/or bulge emission (e.g., Koyama et al. 2007b; Yuasa et al. 2012). A total of 29 *Suzaku* pointings (14 from AO7, 4 from AO8, and 11 from archival data) are analyzed in this paper. Note that five of these archival data sets are located near the N-cap area and were published in 2015 as "N-cap1–5." Table 1 summarizes all the times of the exposures and directions of the pointing centers of the *Suzaku* data sets used in this paper. The *Suzaku* pointing positions (focal centers) are overlaid as green or red circles onto the *ROSAT* 0.75 keV image in Figure 1, with the boundary of the Fermi bubbles as drawn by Su et al. (2010) indicated.

We conducted all data reduction with the same methods as described in detail in Papers I and II using the HEADAS software version 6.14 and the calibration database (CALDB) released on 2013 August 13. In summary, using `XSELECT`, the data corresponding to epochs of (i) low-Earth elevation angles (less than 20° during both night and day), (ii) the South Atlantic Anomaly (and 500 s after), and (iii) the low cutoff rigidity of below 6 GV were excluded. Hot and flickering pixels were removed using `SISCLEAN` (Day 1998). Final images were created after the non-X-ray background (NXB) created with `XISNXBGEN` (Tawa et al. 2008) was subtracted from the raw XIS 0.4–10 keV images and a vignetting correction was applied using simulated flat-sky images from `XISSIM` (Ishisaki et al. 2007).

2.2. Swift XRT

Swift (Gehrels et al. 2004) is an observatory mission whose primary goal is to explore and follow-up gamma-ray bursts. Its high mobility and sensitivity to localize sources especially using its XRT (Burrows et al. 2005) make it valuable for monitoring various X-ray sources within short exposures of typically $\leqslant$5 ks. The field of view of *Swift* XRT is $23\farcm6 \times 23\farcm6$, and the telescope HPD is $18''$ at 1.5 keV. While we did not conduct any dedicated *Swift* pointings of the Fermi bubbles as we did with *Suzaku*, we found many short *Swift* pointings in the Fermi bubbles' direction, namely, $|l| < 20^\circ$ and $|b| < 60^\circ$. Note that *Swift* also carries an ultraviolet/optical telescope (Roming et al. 2005) and the Burst Alert Telescope (Barthelmy et al. 2005), but we did not use these data because the thermal emission we describe below is too faint to be detected in the optical/ultraviolet and above 15 keV.

We selected *Swift* observation pointings in which (i) no bright sources having XRT count rates of $\geqslant$0.6 counts s^{-1} were found in the same field of view to avoid CCD pileup, and (ii) $|b| > 5^\circ$ to avoid contamination from the GC region and/or bulge emission. This selection yields 68 pointings, which we analyzed in this paper. Note that 19 of the *Swift* archival data sets located in the vicinity of the N-cap area were already analyzed in 2015 as "Swift1–19." Table 2 summarizes the times of the exposures and directions of the pointing center of

Table 1
Suzaku Observation Log

ID	Start Time (UT)	Stop Time (UT)	R.A. (°)[a]	Decl. (°)[b]	l (°)[c]	b (°)[d]	Exposure (ks)[e]	Note[f]
			North Bubble					
507006010	2012 Aug 08 10:23	2012 Aug 08 23:03	233.401	9.076	15.480	47.714	17.5 (45.5)	I (N1)
507005010	2012 Aug 07 23:41	2012 Aug 08 10:22	233.623	8.079	14.388	47.011	16.2 (36.9)	I (N2)
507004010	2012 Aug 07 10:31	2012 Aug 07 23:40	233.834	7.087	13.321	46.308	17.6 (46.2)	I (N3)
507003010	2012 Aug 06 23:20	2012 Aug 07 10:30	234.034	6.098	12.280	45.606	16.7 (40.2)	I (N4)
507001010	2012 Aug 05 23:04	2012 Aug 06 09:33	234.250	5.090	11.255	44.871	15.3 (36.0)	I (N5)
507002010	2012 Aug 06 09:34	2012 Aug 06 23:18	234.405	4.131	10.263	44.204	19.0 (47.9)	I (N6)
507007010	2012 Aug 08 23:06	2012 Aug 09 10:20	234.551	3.174	9.291	43.537	17.0 (40.4)	I (N7)
507008010	2012 Aug 09 10:21	2012 Aug 09 23:53	234.713	2.200	8.334	42.838	12.0 (24.9)	I (N8)
508007010	2013 Jul 26 08:09	2013 Jul 26 20:11	221.750	−1.312	351.952	50.223	20.7 (40.7)	II (N_cap_on)
508008010	2013 Jul 26 20:16	2013 Jul 27 10:14	233.686	−9.893	355.509	35.809	19.6 (48.8)	II (N_cap_off)
807062010	2012 Aug 01 23:39	2012 Aug 02 10:54	217.761	0.794	349.311	54.438	15.3 (40.4)	II (N_cap_1)
807058010	2012 Jul 28 08:10	2012 Jul 28 17:58	233.434	3.616	8.894	44.702	10.4 (38.8)	II (N_cap_2)
705026010	2011 Feb 01 18:51	2011 Feb 02 04:25	230.255	−3.837	358.141	42.451	17.5 (31.7)	II (N_cap_3)
701079010	2006 Jul 19 17:39	2006 Jul 20 15:02	220.569	−17.330	337.266	38.061	32.0 (71.1)	II (N_cap_4)
401001040	2006 Feb 27 20:38	2006 Feb 28 23:00	226.648	−16.180	344.020	35.677	28.7 (94.4)	II (N_cap_5)
			South Bubble					
507013010	2012 Apr 19 14:11	2012 Apr 20 02:44	332.668	−46.192	351.010	−53.100	18.1 (41.2)	I (S1)
507012010	2012 Apr 19 03:15	2012 Apr 19 14:10	331.474	−46.348	351.149	−52.265	11.5 (38.8)	I (S2)
507010010	2012 Apr 18 04:59	2012 Apr 18 16:10	330.278	−46.492	351.281	−51.432	11.2 (38.8)	I (S3)
507009010	2012 Apr 17 16:40	2012 Apr 18 04:58	329.080	−46.624	351.406	−50.602	21.0 (42.5)	I (S4)
507011010	2012 Apr 18 16:12	2012 Apr 19 03:12	327.882	−46.743	351.525	−49.775	18.1 (36.9)	I (S5)
507014010	2012 Apr 20 02:47	2012 Apr 20 14:25	326.683	−46.851	351.638	−48.950	11.1 (40.2)	I (S6)
508009010	2013 Apr 22 16:51	2013 Apr 23 07:56	287.398	−27.250	9.973	−15.747	11.8 (48.8)	II (SE_on)
508010010	2013 Apr 23 07:58	2013 Apr 23 19:59	288.748	−25.775	11.875	−16.290	16.0 (43.1)	II (SE_off)
500003010	2006 Mar 08 17:41	2006 Mar 09 01:07	282.688	−33.893	1.999	−14.596	9.89 (25.2)	BULGE_6
100041020	2006 Mar 23 22:31	2006 Mar 25 10:38	284.147	−37.910	−1.403	−17.211	63.5 (129)	RXJ1856
705014010	2010 Apr 13 06:37	2010 Apr 14 00:08	285.522	−51.170	−14.421	−22.401	23.0 (58.7)	EMS1274
705028010	2010 Oct 28 10:57	2010 Oct 29 03:19	309.873	−56.354	−18.821	−37.128	15.9 (58.7)	EMS1388
806079010	2011 May 08 23:24	2011 May 10 00:21	319.721	−63.575	−29.263	−40.234	32.9 (83.2)	RCS2118
703012010	2008 May 11 12:28	2008 May 12 13:35	327.081	−34.951	10.029	−50.337	32.7 (89.1)	NGC7130

Notes.
[a] R.A. of *Suzaku* pointing center in J2000 equinox.
[b] Decl. of *Suzaku* pointing center in J2000 equinox.
[c] Galactic longitude of *Suzaku* pointing center.
[d] Galactic latitude of *Suzaku* pointing center.
[e] *Suzaku* XIS exposure in ks that was actually used in the analysis, as compared with total elapsed time for the observation shown in parentheses.
[f] Reference or focusing target of the observations. I and II denote the data from Papers I and II, respectively, that were uniformly reanlyzed here. N1-8, S1-6, N_cap_on, N_cap_on, SE_on, and SE_off denote dedicated observations for the Fermi bubbles conducted in *Suzaku* AO7 and AO8 from Papers I and II, while the remaining are newly analyzed archival data sets.

each *Swift* pointing used in this paper. The *Swift* pointing positions (focal centers) are indicated as green or red crosses in Figure 1. Note that the six *Swift* pointings shown as red crosses exactly coincide with the X-ray enhancements/structures suggested to be associated with the Fermi bubbles, namely, the NPS, SE-claw, or NW-clump as shown in Figure 1.

In the reduction of the *Swift* XRT data, the HEADAS software version 6.14 and the CALDB as of 2014 January 20 were used. In the XRT analysis, we only use the "Photon Counting" (PC) mode data (Hill 2004). We calibrated Level 1 data as recommended by the *Swift* team[6]. Specifically, we selected a good time interval (GTI) from the Level 1 data using `xrtpipeline`, and the temperatures of the CCDs were set to "$\leqq -50$" in the reduction.

3. ANALYSIS AND RESULTS

3.1. Extracting X-Ray Spectra

For the diffuse emission analysis of the *Suzaku* data, we first ran the source detection algorithm in `XIMAGE` (Giommi et al. 1992) to eliminate compact X-ray features from diffuse X-ray emission. We set the source region to the whole CCD chip that remained after excluding all the compact features detected at significance levels above 3σ with typical $2'$ radius circles, enough to avoid the contamination from the compact sources. Then we used all the FI and BI CCDs, namely, XIS0, 1, 3 for the spectral analysis to maximize the photon statistics.

[6] The *Swift* XRT Data Reduction Guide: http://heasarc.nasa.gov/docs/swift/analysis/xrt_swguide_v1_2.pdf

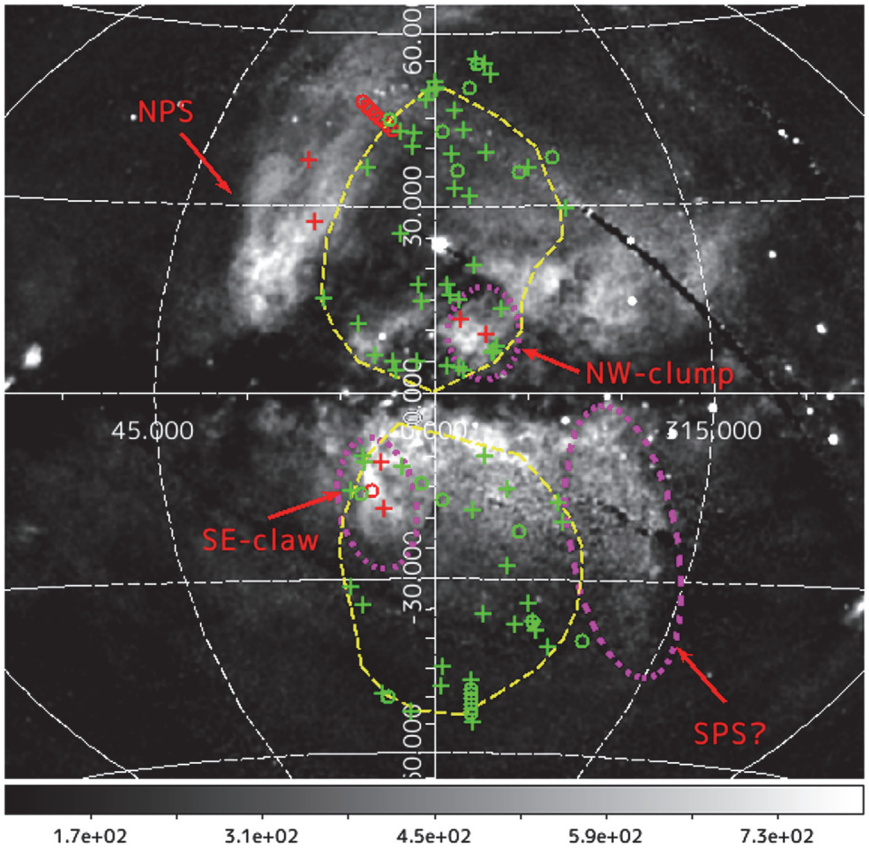

Figure 1. Positions in Galactic coordinates of the 29 *Suzaku* (circles) and 68 *Swift* (crosses) X-ray data field of views systematically analyzed in this paper overlaid on a *ROSAT* 0.75 keV image (grayscale). The pointings within the NPS, SE-claw (an arc-shaped X-ray spur; dashed magenta), and NW-clump (an X-ray clump; dashed magenta) are shown in red, and all others are in green. Yellow dashed lines indicate the boundary of the Fermi bubbles, as suggested in Su et al. (2010).

We made redistribution matrix files (RMFs) using XISRMFGEN (Ishisaki et al. 2007). Auxillary response files (ARFs) were created using XISSIMARFGEN (Ishisaki et al. 2007) and new contamination files (released on 2013 August 13), assuming the uniform extension of the diffuse emission within 20′ radius orbicular regions (giving the ARF area of 0.35 $\deg^2$). We subtracted as background the NXB data obtained from the region in the same CCD chip. Because some of the exposures are short (∼10 ks; Table 1), we carefully checked the analysis results by adopting different choices for source extraction radii and NXB/CXB models, but the results were unchanged within the uncertainties given in Table 3.

Similarly in the *Swift* XRT analysis, we extracted X-ray images in the energy range of 0.5–5 keV using xselect. Exposure maps were made using xrtexpomap. We ran the source detection algorithm in XIMAGE and searched for X-ray compact features that were detected with photon statistics at >3σ confidence levels over the background. In the XRT spectral analysis of the diffuse emission, PHA files were extracted from event files with xselect. We made ARFs using xrtmkarf, while we used the current RMFs in CALDB. To extract photons from diffuse X-ray emission only, we eliminated all the point sources using circles of 30″ radius.

In contrast to *Suzaku* data, evaluation of the instrumental background (NXB) is not well established for the *Swift* XRT data, and studies are still ongoing (e.g., Moretti et al. 2009, 2011, 2012). However, as shown in Moretti et al. (2011, Figure 5 therein), the contribution of the NXB with respect to the CXB is less than 20% below 2 keV and gradually increases to $\gtrsim$50% at above 5 keV. Given that each *Swift* pointing (Table 2) is typically less than 10 ks and thus too short to derive meaningful spectra above 5 keV, we did not use the data above 5 keV for the spectral fitting. Moreover, we modeled the total XRT background as the sum of the NXB and CXB and checked that the analysis results for the diffuse emission were unchanged (within 1σ uncertainty; see the next section) when changing the upper boundary to either 5 keV or 2 keV in the spectral fitting.

3.2. Diffuse X-Ray Emission

Following Papers I and II, all the spectra of the *Suzaku* and *Swift* pointings after removing compact X-ray sources were fitted with a three-component plasma model APEC1 + WABS* (APEC2 + PL) using XSPEC. The model consists of an *unabsorbed* thermal component (denoted as APEC1) that represents the Local Bubble emission and/or contamination from the Solar-Wind Charge Exchange (SWCX; Fujimoto et al. 2007), an *absorbed* thermal component (denoted as APEC2) representing the GH, and a single power-law component (denoted as PL) corresponding to the isotropic CXB radiation together with instrumental background for the case of *Swift* XRT. The photon index for the CXB component was fixed at $\Gamma_{\rm CXB} = 1.41$ (Kushino et al. 2002). The temperature and abundance of the LB plasma were fixed at $kT = 0.1$ keV and $Z = Z_{\odot}$, respectively, as we did in Papers I and II (see also, e.g., Yoshino et al. 2009; Henley & Shelton 2013).

Table 2
Swift Observation Log

ID	Start Time (UT)	Stop Time (UT)	R.A. (°)[a]	Decl. (°)[b]	l (°)[c]	b (°)[d]	Exposure (ks)[e]	Note[f]
			North Bubble					
00037600001	2009 Dec 19 01:45	2009 Dec 19 08:34	217.296	1.301	349.261	55.125	5.42 (24.7)	II (Swift1)
00037755001	2009 Dec 18 03:11	2009 Dec 18 16:14	216.922	0.005	347.337	54.359	7.59 (47.0)	II (Swift2)
00091308008	2013 Mar 26 06:42	2013 Mar 26 11:56	217.608	−1.829	346.343	52.493	4.57 (18.9)	II (Swift3)
00082093002	2013 Sep 12 14:18	2013 Sep 12 22:12	224.263	2.802	359.375	51.352	2.62 (28.5)	II (Swift4)
00032864005	2013 Jun 30 05:36	2013 Jun 30 18:46	224.975	1.894	359.016	50.216	5.49 (47.4)	II (Swift5)
00033207001	2014 Mar 28 00:14	2014 Mar 28 17:27	225.232	1.908	359.351	50.035	8.72 (62.0)	II (Swift6)
00033265002	2014 Apr 28 10:56	2014 Apr 28 12:39	226.089	2.310	0.777	49.575	2.98 (6.17)	II (Swift7)
00090306002	2010 Dec 25 16:19	2010 Dec 25 18:07	227.614	1.755	1.577	48.145	1.56 (6.51)	II (Swift8)
00090281001	2010 Apr 08 10:32	2010 Apr 08 13:55	226.089	−2.597	355.346	46.306	2.17 (12.2)	II (Swift9)
00036338003	2008 Jan 07 13:54	2008 Jan 07 23:44	227.732	−5.725	353.912	42.925	5.01 (35.4)	II (Swift10)
00039721001	2010 Dec 29 00:45	2010 Dec 30 17:04	234.249	0.959	6.602	42.472	5.14 (145)	II (Swift11)
00037942001	2008 Jun 22 07:20	2008 Jun 22 14:02	233.223	−0.749	3.927	42.230	5.21 (24.2)	II (Swift12)
00039723001	2011 Jan 02 01:06	2011 Jan 02 06:16	235.090	−2.041	4.141	39.966	5.26 (18.6)	II (Swift13)
00040980001	2010 Sep 16 01:01	2010 Sep 16 07:44	228.007	−10.863	349.572	38.957	5.44 (24.2)	II (Swift14)
00055750014	2011 Jan 14 03:35	2011 Jan 14 07:05	232.086	−7.240	356.528	38.790	2.56 (12.7)	II (Swift15)
00035800002	2006 Oct 08 16:10	2006 Oct 09 05:09	245.412	9.558	23.816	37.542	4.58 (46.8)	II (Swift16)
00037281001	2008 Jan 20 00:44	2008 Jan 20 16:59	241.792	1.112	12.405	36.399	8.69 (58.5)	II (Swift17)
00037279002	2008 Dec 26 00:03	2008 Dec 27 22:53	224.853	−16.693	341.960	36.300	8.52 (169)	MASER1459
00036065002	2007 Jan 17 00:55	2007 Jan 17 23:33	236.199	−11.491	356.179	32.920	6.16 (81.5)	II (Swift18)
00038072003	2010 Jan 07 10:10	2010 Jan 07 22:58	235.510	−14.168	353.354	31.538	7.87 (46.1)	J1542
00041776003	2011 Mar 27 08:19	2011 Mar 27 19:52	224.702	−24.950	336.289	29.547	7.05 (41.6)	J1458
00037283001	2008 Jan 20 18:24	2008 Jan 21 13:46	253.272	2.403	20.746	27.269	8.03 (69.7)	II (Swift19)
00037188002	2008 Jan 16 00:15	2008 Jan 16 22:59	247.263	−9.882	5.589	25.601	10.7 (81.8)	J1629
00090500002	2010 Jul 06 04:13	2010 Jul 06 12:36	243.873	−22.205	353.022	20.248	5.72 (30.2)	UKSCE-1
00046310001	2013 Jan 31 01:37	2013 Jan 31 08:07	252.202	−17.317	2.269	17.310	4.30 (23.4)	PBCJ1648
00036649002	2007 Oct 08 03:07	2007 Oct 08 14:31	249.626	−20.944	357.709	17.010	4.59 (41.1)	IGRJ1638
00041223001	2010 Sep 28 08:24	2010 Sep 28 15:27	250.605	−22.371	357.144	15.407	4.72 (25.4)	IGRJ1642
00035086002	2007 Feb 24 00:06	2007 Feb 24 14:40	262.590	−5.9926	17.929	15.013	12.7 (52.8)	IGRJ1730
00037644001	2009 Feb 24 10:48	2009 Feb 24 17:16	250.075	−23.896	355.599	14.827	3.46 (23.3)	HD150193
00090182002	2010 Jan 23 11:43	2010 Jan 23 23:06	253.660	−19.269	1.496	15.034	3.98 (41.0)	J1654
00038075002	2010 Jan 23 02:04	2010 Jan 23 10:15	246.613	−29.856	348.871	13.260	4.67 (29.5)	J1626
00090991002	2011 Feb 02 04:01	2011 Feb 02 23:34	252.873	−26.009	355.535	11.526	8.90 (70.4)	AS210
00036347001	2007 Feb 27 00:16	2007 Feb 27 15:02	263.261	−13.080	12.032	10.812	10.7 (53.0)	MOJ2B1730
00035348002	2006 Feb 03 00:04	2006 Feb 03 22:53	252.047	−30.599	351.430	9.223	9.21 (82.1)	IGRJ1648
00036118001	2007 Jan 27 16:12	2007 Jan 28 00:23	252.505	−33.116	349.710	7.330	4.60 (29.5)	IGRJ1650
00035647002	2007 Feb 06 01:23	2007 Feb 06 23:59	253.794	−33.162	350.355	6.460	6.95 (81.4)	J1655
00035272002	2006 Jun 13 16:39	2006 Jun 13 21:50	254.072	−33.079	350.567	6.330	4.79 (18.7)	J1656
00037646002	2010 Nov 02 03:49	2010 Nov 02 05:42	266.309	−17.946	9.364	5.779	1.88 (6.80)	GLMP632
00036121001	2007 Feb 27 16:20	2007 Feb 27 23:03	263.283	−24.113	2.606	4.928	6.12 (24.2)	IGRJ1733
00031277001	2008 Oct 16 06:10	2008 Oct 16 23:55	265.538	−20.916	6.435	4.861	4.35 (63.9)	J1741
			South Bubble					
00091760004	2013 Nov 06 02:50	2013 Nov 06 11:02	272.290	−41.224	351.638	−10.236	3.79 (29.5)	AS276
00031677002	2010 Nov 03 08:36	2010 Nov 03 23:27	282.418	−23.811	11.316	−10.242	3.79 (53.5)	ROSS154
00090992004	2010 Nov 06 04:06	2010 Nov 06 20:17	283.279	−24.328	11.178	−11.174	5.07 (58.3)	AS327
00048048002	2012 May 06 03:53	2012 May 07 17:05	282.008	−26.841	8.363	−11.191	3.36 (134)	PBCJ1847
00036632002	2007 Aug 05 08:26	2007 Aug 05 19:48	281.304	−30.254	4.933	−12.056	5.12 (41.0)	J1845
00035794001	2007 Jun 19 17:48	2007 Jun 19 22:52	276.781	−46.941	347.751	−15.594	3.37 (18.3)	XMMSL1J1827
00036405001	2008 May 30 08:56	2008 May 31 23:45	288.888	−24.179	13.456	−15.786	7.15 (140)	HD1799
00036289001	2007 Apr 08 01:13	2007 Apr 08 09:25	274.940	−55.356	339.182	−17.784	3.15 (29.6)	J1819
00040716003	2010 Aug 25 00:45	2010 Aug 25 12:13	289.868	−29.974	8.178	−18.777	4.47 (41.3)	PBCJ1919
00035839001	2007 Apr 27 11:09	2007 Apr 27 19:32	284.035	−43.056	353.500	−18.944	4.06 (30.2)	XMMSL1J1856
00038080002	2008 Nov 02 01:10	2008 Nov 02 11:12	279.767	−57.281	338.240	−20.958	8.35 (36.1)	SWIFTJ1839
00031727001	2010 May 26 10:13	2010 May 26 15:13	285.522	−51.170	345.578	−22.404	4.24 (18.0)	1FGLJ1902
00041100002	2010 Jun 11 05:10	2010 Jun 11 23:09	294.536	−51.136	346.988	−27.909	7.03 (64.8)	SWIFTJ1938
00032516006	2012 Jul 22 14:55	2012 Jul 23 06:57	305.912	−28.278	14.862	−31.529	3.92 (57.8)	PSNJ2023
00037330002	2008 Jun 18 01:24	2008 Jun 18 23:59	304.610	−55.650	342.270	−34.232	5.82 (81.3)	SWIFTJ2018
00041108001	2010 Dec 02 06:32	2010 Dec 02 21:16	308.602	−30.602	12.905	−34.391	7.39 (53.0)	SWIFTJ2034

Table 2
(Continued)

ID	Start Time (UT)	Stop Time (UT)	R.A. (°)[a]	Decl. (°)[b]	l (°)[c]	b (°)[d]	Exposure (ks)[e]	Note[f]
00035790004	2007 Mar 30 00:05	2007 Mar 30 08:41	307.684	−48.788	350.669	−36.101	3.78 (31.0)	XMMSL1J2030
00041479002	2011 Feb 21 02:29	2011 Feb 21 11:59	309.873	−56.354	341.182	−37.125	3.61 (34.2)	1FGLJ2039
00046327002	2012 Jun 20 01:54	2012 Jun 20 23:01	310.648	−53.695	344.465	−37.817	3.85 (76.0)	PBCJ2042
00080269001	2013 Jul 08 07:35	2013 Jul 08 16:12	313.008	−57.069	339.991	−38.735	7.12 (31.1)	PBCJ2052
00091684001	2013 Apr 02 01:19	2013 Apr 02 23:51	313.072	−57.064	339.991	−38.770	4.78 (81.2)	SWIFTJ2052
00041188004	2011 Jul 02 23:29	2011 Jul 03 22:21	319.007	−58.662	337.033	−41.490	5.12 (82.4)	SWIFTJ2116
00035232001	2005 Dec 07 00:22	2005 Dec 07 23:10	320.308	−43.007	358.079	−44.971	9.68 (82.1)	SWIFTJ2121
00033015009	2014 Apr 01 14:34	2014 Apr 01 23:01	324.363	−47.032	351.833	−47.361	4.29 (30.4)	ESO287
00038411002	2009 Apr 05 14:50	2009 Apr 06 07:01	324.850	−42.589	358.318	−48.326	6.41 (58.3)	MH2136
00039206001	2009 Sep 22 08:10	2009 Sep 22 13:26	326.255	−33.955	11.447	−49.629	6.58 (19.0)	PMNJ2145
00037292001	2008 Apr 06 06:55	2008 Apr 07 15:12	330.321	−37.773	5.315	−52.906	11.1 (116)	MASER2201
00040395004	2012 Sep 25 04:02	2012 Sep 25 23:31	335.239	−46.036	350.319	−54.843	9.51 (70.2)	IC5201

Notes.
[a] Right ascension of *Swift* pointing center in J2000 equinox.
[b] Declination of *Swift* pointing center in J2000 equinox.
[c] Galactic longitude of *Swift* pointing center.
[d] Galactic latitude of *Swift* pointing center.
[e] *Swift* XRT exposure in ks that was actually used in the analysis, as compared with total elapsed time for the observation shown in parentheses.
[f] Reference or focusing target. II denotes data presented in Paper II and uniformly reanalyzed here, while the rest are newly presented in this paper.

As for the absorbed diffuse emission, the neutral hydrogen column density was fixed to the Galactic value $N_{\rm H,\,Gal}$ in the direction of each pointing because most of the values are consistent with the full Galactic values when $N_{\rm H}$ was left free in the spectral fitting. We also fixed the abundance of the APEC2 at $Z = 0.2\,Z_{\odot}$, which is the on-average preferred value as detailed in Appendix B of Paper I. This level of sub-solar metallicity is also supported by a recent study of the GH using the *XMM-Newton* Reflection Grating Spectrometer, which measured the O VII K_{α} absorption line (Miller & Bregman 2013; but see, e.g., Yao et al. 2008 and Yoshino et al. 2009, who assumed $Z = Z_{\odot}$). Even after reducing free parameters in the spectral fitting as described above, the photon statistics are too low to derive individual spectra for the 68 *Swift* XRT pointings, except for six regions positioned at the bright X-ray enhancements denoted as the NPS, NW-clump, and SE-claw in Figure 1. We therefore generated a spectrum by stacking *Swift* XRT data typically every 5° in Galactic latitude ($\Delta b \simeq 5°$ −15°) to increase the photon statistics. The results of our spectral fitting obtained for the *Suzaku* data and *Swift* data are summarized in Tables 3 and 4, respectively. In both tables, "PL norm" represents the power-law intensity as measured in 2 −10 keV, normalized by the absolute intensity of the CXB, namely, $(5.85 \pm 0.38) \times 10^{-8}$ erg cm^{-2} s^{-1} sr^{-1} (Kushino et al. 2002). The value is close to unity for the *Suzaku* data, with some variations expected from the large-scale fluctuation of the CXB itself. The slightly larger values of PL norm in the *Swift* data indicate a non-negligible contribution from the NXB in this energy band, as mentioned above.

3.3. EM and kT Distributions along Galactic Latitude

As can be seen in Tables 3 and 4, the temperature of the GH as modeled by APEC2 is well represented by $kT \simeq 0.3$ keV, while the EM widely spans an order of magnitude depending on the Galactic latitude. To view the trend more clearly, Figure 2 shows the variations of EM (top panel) and kT (bottom panel) for the APEC2 emission component as a function of Galactic latitude b for all the *Suzaku* and *Swift* data. Red filled circles indicate X-ray enhancements corresponding to the NPS, NW-clump, and SE-claw, as also marked in red in Figure 1. One can see that the temperature is surprisingly uniform over a wide range of Galactic latitude $5° \lesssim |b| < 60°$ with fluctuations in kT of only 0.30 ± 0.07 keV over the whole spatial extent of the Fermi bubbles.

While the temperature values are uniform, the EM values increase steeply toward the GC (i.e., low $|b|$) with sudden jumps possibly related to the X-ray enhancements near the Fermi bubbles' edges. Moreover, the EM distribution is asymmetric with respect to the Galactic plane, decreasing more gradually in the north ($b > 0°$) than in the south ($b < 0°$) toward high Galactic latitudes. For example, EM at $20° < b < 35°$, $(5.82 \pm 0.76) \times 10^{-2}$ cm^{-6} pc, is more than a factor of two larger than the corresponding EM in the south, where $(2.52\,^{+1.10}_{-0.52}) \times 10^{-2}$ cm^{-6} pc at $-35° < b < -25°$. The origin of this asymmetry is discussed in more detail in the following section.

4. DISCUSSION

Following Papers I and II, we continued our systematic analysis of diffuse X-ray emission possibly related with the Fermi bubbles using data from both *Suzaku* and *Swift*. The X-ray data analyzed here were collected from archival observations covering Galactic longitude $|l| < 20°$ and latitude $5° \lesssim |b| < 60°$, approximately coinciding with the spatial extent of the Fermi bubbles. We showed that (i) the temperature of the GH is uniform along Galactic latitude with $kT \simeq 0.30 \pm 0.07$ keV; (ii) the EM, in contrast, varies widely by more than an order of magnitude, with its values gradually decreasing toward high b; and (iii) the distribution of EM is asymmetric between the north and south bubbles. While the north/south asymmetry is evident in the *ROSAT* 0.75 keV image (Snowden et al. 1995), we showed for the first time that this is mainly accounted for by variations in the EM rather than differences in

Table 3
Fitting Parameters for *Suzaku* Observations

ID	$N_{\rm H,\,Gal}$[a] (10^{20} cm^{-2})	kT_1[b] (keV)	$\rm EM_1$[c] (10^{-2} cm^{-6} pc)	kT_2[d] (keV)	$\rm EM_2$[e] (10^{-2} cm^{-6} pc)	PL Norm[f]	χ^2/dof
North Bubble							
N1	3.37	0.1(fix)	5.76 ± 1.05	$0.304^{+0.019}_{-0.015}$	6.12 ± 0.71	1.02 ± 0.06	189.28/155
N2	3.83	0.1(fix)	5.66 ± 1.03	$0.320^{+0.021}_{-0.017}$	5.96 ± 0.71	1.01 ± 0.07	171.73/155
N3	3.86	0.1(fix)	$0.36^{+6.51}_{-0.36}$	$0.297^{+0.029}_{-0.013}$	$7.22^{+0.80}_{-1.47}$	1.08 ± 0.08	172.51/146
N4	4.06	0.1(fix)	6.78 ± 1.10	$0.310^{+0.021}_{-0.017}$	6.17 ± 0.76	0.69 ± 0.06	225.82/155
N5	4.26	0.1(fix)	$5.28^{+1.07}_{-1.24}$	$0.280^{+0.016}_{-0.021}$	$6.35^{+1.24}_{-0.76}$	0.88 ± 0.07	153.12/155
N6	4.45	0.1(fix)	7.24 ± 1.05	$0.304^{+0.026}_{-0.020}$	4.36 ± 0.68	1.01 ± 0.06	169.60/155
N7	4.76	0.1(fix)	5.81 ± 0.95	$0.282^{+0.018}_{-0.022}$	$5.23^{+1.06}_{-0.67}$	0.62 ± 0.05	171.31/155
N8	5.02	0.1(fix)	6.05 ± 0.93	0.284 ± 0.022	$4.28^{+0.84}_{-0.65}$	0.82 ± 0.06	172.76/155
N_cap_on	4.12	0.1(fix)	3.70 ± 0.99	$0.307^{+0.074}_{-0.031}$	$2.33^{+0.59}_{-0.71}$	0.96 ± 0.07	187.91/149
N_cap_off	10.69	0.1(fix)	3.85 ± 0.86	$0.299^{+0.025}_{-0.019}$	4.94 ± 0.76	0.82 ± 0.06	142.05/148
N_cap_1	3.02	0.1(fix)	$1.80^{+1.40}_{-1.39}$	$0.245^{+0.052}_{-0.026}$	$2.95^{+1.17}_{-1.08}$	0.81 ± 0.06	191.18/150
N_cap_2	4.27	0.1(fix)	$6.13^{+1.90}_{-2.29}$	$0.360^{+0.309}_{-0.062}$	$4.00^{+1.11}_{-2.39}$	0.99 ± 0.13	152.37/150
N_cap_3	7.47	0.1(fix)	2.28 ± 0.97	$0.303^{+0.029}_{-0.022}$	4.31 ± 0.75	0.92 ± 0.07	197.40/150
N_cap_4	7.82	0.1(fix)	1.49 ± 0.46	$0.303^{+0.017}_{-0.015}$	4.12 ± 0.44	0.81 ± 0.05	168.41/150
N_cap_5	8.11	0.1(fix)	2.01 ± 0.51	$0.289^{+0.013}_{-0.011}$	5.89 ± 0.54	0.77 ± 0.06	161.25/149
South Bubble							
S1	1.84	0.1(fix)	$4.31^{+1.10}_{-1.47}$	$0.283^{+0.246}_{-0.082}$	$0.87^{+1.27}_{-0.54}$	0.90 ± 0.07	156.53/142
S2	1.66	0.1(fix)	$4.09^{+1.03}_{-1.15}$	$0.281^{+0.111}_{-0.056}$	$1.08^{+0.81}_{-0.51}$	0.94 ± 0.07	178.68/152
S3	1.89	0.1(fix)	3.63 ± 0.57	0.350 ± 0.078	0.90 ± 0.30	0.91 ± 0.05	201.77/154
S4	2.16	0.1(fix)	$5.03^{+0.86}_{-0.97}$	$0.334^{+0.104}_{-0.060}$	$1.00^{+0.49}_{-0.36}$	$0.97^{+0.07}_{-0.06}$	180.01/152
S5	2.45	0.1(fix)	$4.88^{+0.93}_{-1.07}$	$0.256^{+0.063}_{-0.040}$	$1.40^{+0.85}_{-0.55}$	0.86 ± 0.05	188.60/155
S6	3.03	0.1(fix)	$4.78^{+1.55}_{-2.28}$	$0.233^{+0.107}_{-0.053}$	$1.89^{+2.97}_{-0.71}$	0.69 ± 0.07	186.88/148
SE_on	11.87	0.1(fix)	9.48 ± 1.85	$0.300^{+0.009}_{-0.008}$	28.3 ± 1.87	0.65 ± 0.08	192.06/150
SE_off	11.56	0.1(fix)	7.00 ± 1.19	$0.300^{+0.014}_{-0.012}$	11.6 ± 1.09	0.82 ± 0.06	178.33/150
BULGE_6	10.50	0.1(fix)	5.12 ± 0.90	$0.296^{+0.012}_{-0.011}$	11.5 ± 0.97	0.70 ± 0.07	163.92/149
RXJ1856	9.01	0.1(fix)	3.01 ± 0.51	$0.295^{+0.012}_{-0.010}$	7.22 ± 0.56	0.92 ± 0.07	182.59/149
EMS1274	5.59	0.1(fix)	3.71 ± 0.91	$0.290^{+0.013}_{-0.011}$	6.54 ± 0.62	0.89 ± 0.05	208.41/149
EMS1388	5.23	0.1(fix)	$1.91^{+0.99}_{-1.27}$	$0.281^{+0.069}_{-0.054}$	$1.65^{+1.16}_{-0.61}$	0.80 ± 0.07	207.34/149
RCS2118	2.97	0.1(fix)	3.26 ± 0.81	$0.307^{+0.041}_{-0.027}$	1.92 ± 0.41	0.73 ± 0.05	176.40/149
NGC7130	2.10	0.1(fix)	$1.94^{+0.60}_{-0.61}$	$0.308^{+0.102}_{-0.058}$	$0.71^{+0.37}_{-0.28}$	0.74 ± 0.05	194.91/149

Notes.
[a] The absorption column densities for the CXB and the GH/NPS components (WABS*(APEC2 + PL)) were fixed to Galactic values given in Dickey & Lockman (1990).
[b] Temperature of the LB/SWCX plasma fitted with the APEC model for the fixed abundance $Z = Z_\odot$.
[c] Emission measure of the LB/SWCX plasma fitted with the APEC model for the fixed abundance $Z = Z_\odot$.
[d] Temperature of the GH/NPS plasma fitted with the APEC model for the fixed abundance $Z = 0.2\,Z_\odot$.
[e] Emission measure of the GH/NPS plasma fitted with the APEC model for the fixed abundance $Z = 0.2\,Z_\odot$.
[f] The normalization of the PL in units of 5.85×10^{-8} erg cm^{-2} s^{-1} sr^{-1}, given in Kushino et al. (2002) as an average of 91 observation fields, assuming a single power-law model with a photon index $\Gamma_{\rm CXB} = 1.41$.

plasma temperature kT that emits $\simeq$0.75 keV X-rays. The observed kT is a bit higher than what was derived for Galactic longitudes $65° < l < 295°$ (Yoshino et al. 2009) and $120° < l < 240°$ (Henley et al. 2010; Henley & Shelton 2013), regions that are well outside the bubbles' region, and hence was regarded as evidence of weak-shock heating during the bubble's expansion (Papers I and II). Although it is still unclear whether the observed $kT \simeq 0.3$ keV plasma is really associated with the bubbles (see discussion in Paper I), we are particularly interested in the global structure and asymmetry of EM ((ii) and (iii) described above) in order to further understand the possible relation between the observed $kT \simeq 0.3$ keV plasma and the Fermi bubbles.

4.1. A Model of the Bubbles in the GH

Here we assume a simple model in which two spherical bubbles, which mimic the north and south Fermi bubbles, are embedded in the center of a gaseous halo with radius $R_{\rm h}$ (kpc). We set the GC at the origin of Cartesian space, and the Galactic disk is placed on the xy-plane with the Sun (i.e., observer) positioned at (8 kpc, 0, 0).

As the underlying halo gas density profile, we assume a hydrostatic isothermal model (King profile or β model; King 1962; Cavaliere & Fusco-Femiano 1976) that follows

$$n(r) = n_0\Big(1 + (r/r_{\rm c})^2\Big)^{-3\beta/2}, \quad (1)$$

Table 4
Fitting Parameters for *Swift* Observations

ID	$N_{H,\,Gal}$[a] (10^{20} cm^{-2})	kT_1[b] (keV)	EM_1[c] (10^{-2} cm^{-6} pc)	kT_2[d] (keV)	EM_2[e] (10^{-2} cm^{-6} pc)	PL Norm[f]	χ^2/dof
North Bubble							
$50°< b < 55°$	3.67	0.1(fix)	$2.87^{+0.51}_{-0.54}$	$0.327^{+0.067}_{-0.037}$	$2.05^{+0.48}_{-0.47}$	$1.73^{+0.12}_{-0.13}$	41.24/27
$45°< b < 50°$	4.71	0.1(fix)	$4.24^{+1.11}_{-1.19}$	$0.273^{+0.051}_{-0.033}$	$3.60^{+1.34}_{-1.07}$	$2.25^{+0.18}_{-0.19}$	58.97/39
$40°< b < 45°$	4.71	0.1(fix)	$2.08^{+0.73}_{-0.76}$	$0.294^{+0.052}_{-0.038}$	$2.86^{+0.84}_{-0.73}$	2.03 ± 0.13	54.01/39
$35°< b < 40°$	7.84	0.1(fix)	$2.54^{+0.52}_{-0.60}$	0.273 ± 0.023	$4.24^{+0.93}_{-0.65}$	1.96 ± 0.10	58.68/39
$20°< b < 35°$	11.16	0.1(fix)	2.64 ± 0.47	$0.294^{+0.023}_{-0.018}$	5.82 ± 0.76	1.60 ± 0.14	40.23/27
$15°< b < 20°$	12.83	0.1(fix)	$1.25^{+0.62}_{-0.66}$	$0.277^{+0.026}_{-0.023}$	$7.11^{+1.49}_{-1.19}$	2.01 ± 0.14	58.15/39
$10°< b < 15°$	14.79	0.1(fix)	1.20 ± 0.44	$0.315^{+0.022}_{-0.018}$	8.65 ± 0.99	1.81 ± 0.17	53.35/26
$5°< b < 10°$	24.74	0.1(fix)	1.86 ± 0.56	$0.287^{+0.026}_{-0.021}$	$14.6^{+2.60}_{-2.41}$	2.73 ± 0.18	44.93/39
Swift16 (NPS)	4.50	0.1(fix)	5.46 ± 1.99	$0.303^{+0.053}_{-0.036}$	$7.38^{+1.99}_{-1.92}$	1.82 ± 0.24	44.01/39
Swift19 (NPS)	5.70	0.1(fix)	4.08 ± 1.74	$0.291^{+0.028}_{-0.023}$	12.1 ± 2.00	2.03 ± 0.22	50.58/39
AS210 (NW-clump)	15.79	0.1(fix)	2.73 ± 1.01	$0.294^{+0.020}_{-0.016}$	20.4 ± 2.51	1.94 ± 0.19	63.09/39
IGRJ1648 (NW-clump)	17.56	0.1(fix)	1.91 ± 1.12	$0.299^{+0.026}_{-0.020}$	21.7 ± 3.21	2.73 ± 0.26	54.79/39
South Bubble							
$-15°< b < -10°$	13.51	0.1(fix)	3.81 ± 0.76	$0.312^{+0.019}_{-0.015}$	14.8 ± 1.52	2.21 ± 0.13	85.64/39
$-20°< b < -15°$	8.66	0.1(fix)	$3.54^{+1.21}_{-1.25}$	$0.289^{+0.034}_{-0.026}$	$8.29^{+1.88}_{-1.66}$	2.03 ± 0.19	37.91/39
$-25°< b < -20°$	6.77	0.1(fix)	$1.67^{+0.76}_{-0.82}$	$0.273^{+0.016}_{-0.016}$	$7.80^{+1.16}_{-0.92}$	1.98 ± 0.13	49.11/39
$-35°< b < -25°$	5.41	0.1(fix)	$2.21^{+0.50}_{-0.83}$	$0.268^{+0.029}_{-0.038}$	$2.52^{+1.10}_{-0.52}$	2.01 ± 0.10	64.90/39
$-45°< b < -35°$	5.16	0.1(fix)	$2.35^{+0.46}_{-0.78}$	$0.267^{+0.026}_{-0.038}$	$2.29^{+1.00}_{-0.46}$	$2.14^{+0.10}_{-0.09}$	62.04/39
$-50°< b < -45°$	3.04	0.1(fix)	$1.63^{+0.60}_{-0.78}$	$0.247^{+0.052}_{-0.042}$	$1.65^{+0.94}_{-0.59}$	1.80 ± 0.09	57.65/39
$-55°< b < -50°$	1.56	0.1(fix)	$1.87^{+0.68}_{-1.17}$	$0.233^{+0.110}_{-0.059}$	$0.89^{+1.45}_{-0.55}$	$1.70^{+0.10}_{-0.11}$	51.25/39
PBCJ1847 (SE-claw)	14.71	0.1(fix)	$2.38^{+1.78}_{-1.79}$	$0.323^{+0.030}_{-0.025}$	$24.6^{+4.15}_{-3.78}$	1.72 ± 0.30	46.53/39
PBCJ1919 (SE-claw)	9.13	0.1(fix)	2.57 ± 1.79	$0.306^{+0.042}_{-0.029}$	$12.9^{+2.75}_{-2.72}$	2.21 ± 0.28	50.78/39

Note.
[a] The absorption column densities for the CXB and the GH/NPS components (WABS*(APEC2 + PL)) were fixed to Galactic values given in Dickey & Lockman (1990).
[b] Temperature of the LB/SWCX plasma fitted with the APEC model for the fixed abundance $Z = Z_\odot$.
[c] Emission measure of the LB/SWCX plasma fitted with the APEC model for the fixed abundance $Z = Z_\odot$.
[d] Temperature of the GH/NPS plasma fitted with the APEC model for the fixed abundance $Z = 0.2\,Z_\odot$.
[e] Emission measure of the GH/NPS plasma fitted with the APEC model for the fixed abundance $Z = 0.2\,Z_\odot$.
[f] The normalization of the CXB in units of 5.85×10^{-8} erg cm^{-2} s^{-1} sr^{-1}, given in Kushino et al. (2002) as an average of 91 observation fields, assuming a single power-law model with a photon index $\Gamma_{CXB} = 1.41$.

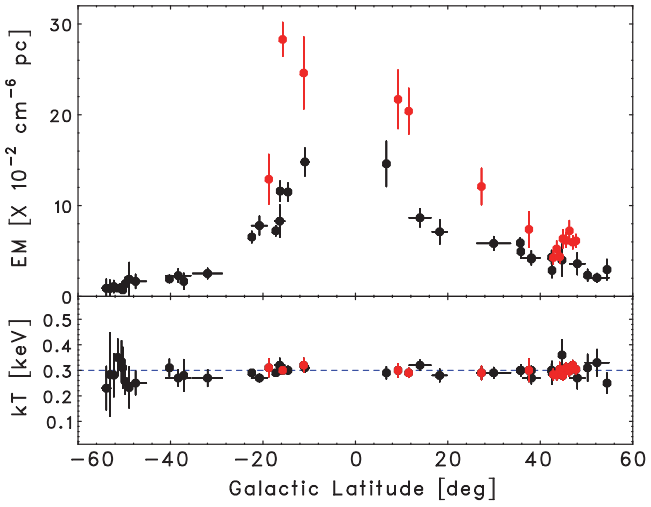

Figure 2. Variation in the spectral fitting parameters EM (top) and kT (bottom) for the APEC2 emission component as a function of Galactic latitude b. Abundances are fixed at $Z = 0.2\,Z_\odot$. The parameters determined for the NPS, SE-claw, and NW-clump are shown in red (see Figure 1).

where $n(r)$ is the gas density in cm^{-3} at radius r from the GC, n_0 is the density at $r = 0$, r_c is the core radius, and β is the slope of the profile at large radii. Following recent studies of the structure of the GH based on X-ray data (e.g., Miller & Bregman 2013), we hereafter set $r_c = 0.5$ kpc and $\beta = 2/3$ in this paper[7]. We also assume the halo boundary at $R_h = 15$ kpc for the purpose of this calculation.

We first calculated the EM profile of the GH *without* bubbles for a direction of interest (l, b) from the Sun by

$$EM(l, b) \propto \int n(r)^2 ds, \quad (2)$$

where ds is an element of length toward the (l, b) direction ("filled-halo" model). For comparison, we also considered a case in which two bubbles expand in the same halo by sweeping up surrounding halo gas ("bubble-in-halo" model). We assume inner and outer radii of the bubbles, R_{in} and R_{out},

[7] More accurately, Miller & Bregman (2013) provided best-fit parameters $r_c = 0.35^{+0.29}_{-0.27}$ kpc and $\beta = 0.71^{+0.13}_{-0.14}$. We thus set the values to rounded numbers within these uncertainties. Note that $n(r) \propto r^{-2}$ for $r \gg r_c$ when $\beta = 2/3$.

where the centers of the northern and southern bubbles are positioned in the xz-plane (i.e., $y = 0$). For simplicity, we assumed null gas density ($n = 0$) inside each bubble, but the swept-up halo gas is distributed uniformly in shells with thickness $\Delta R = R_{\rm out} - R_{\rm in}$, so that mass is conserved between two models. We remind the reader that a halo profile described above was first assumed by Miller & Bregman (2013) based on the X-ray data *without* considering bubbles; thus, assuming the same profile in both the "filled-halo" and "bubble-in-halo" models may be an oversimplification. Nevertheless, we show that our model can account for the global structure of isothermal diffuse X-ray emission as detailed below. We also assumed an inclination of the northern and southern bubbles against the z-axis given by θ. The top panel of Figure 3 shows a schematic view of the geometry assumed here (a cross-sectional view at $l = 0°$ and $\theta = 10°$), and the bottom panel of Figure 3 shows an example 3D diagram of the gas density profile $n(r)$ in our bubble-in-halo model.

Figure 4 shows the variations of EM thus calculated in the (l, b) plane as observed from the Sun for a filled-halo model without bubbles (panel (a)) and the bubble-in-halo model with various inclination angles from $\theta = 0°$ to 30° (panels (b)–(e)). Figure 5 shows the corresponding variations of EM as a function of Galactic latitude b in the case of a filled halo (magenta) and the bubble-in-halo models (blue), as measured for $l = 0°$. We set $R_{\rm in} = 3$ kpc and $R_{\rm out} = 5$ kpc. Note that EM is normalized to its peak value at $b = 0°$ of the filled-halo model. In the absence of the bubbles, the filled-halo model predicts a sharp decrease of EM toward high Galactic latitudes, such that EM at $b = 60°$ is more than three orders of magnitude smaller than that derived at $b = 0°$. In the case of the bubble-in-halo model, by contrast, there is more structure in the variations in EM, which changes by only about an order of magnitude. Also, one can see that the inclination θ may account for a certain degree of asymmetry in the EM, such that the northern bubble is spatially more extended toward high b than the south bubble, as we see in Figure 4(e) for the case of $\theta = 30°$. However, such a large inclination would similarly produce a high degree of asymmetry in the gamma-ray bubbles, which strongly contradicts with the observations (e.g., Ackermann et al. 2014).

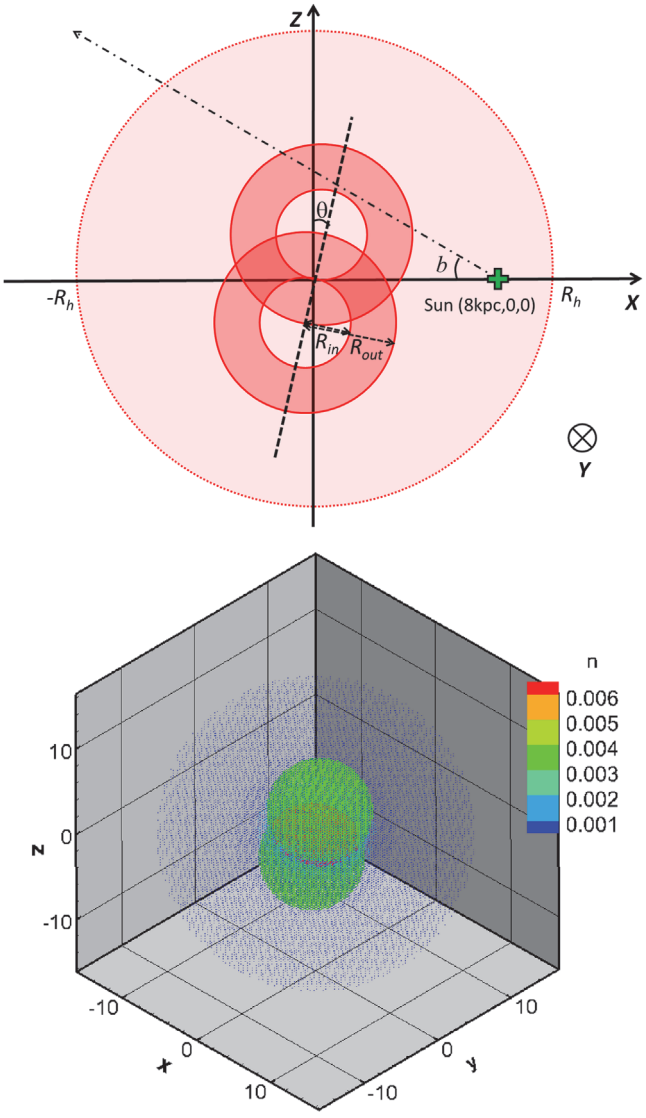

Figure 3. "Bubble-in-halo" model assumed in this paper. As an underlying halo gas density profile, we assumed a β-model as detailed in the text. We set outer radius $R_{\rm out} = 5$ kpc, inner radius $R_{\rm in} = 3$ kpc, and inclination $\theta = 10°$. Top: cross-sectional view at $l = 0°$. Bottom: 3D distribution of gas density profile $n(r)$ in units of cm^{-3}.

4.2. Comparison with Data and Model: The North–South Asymmetry

To determine to what extent the simple models described above can account for the observed EM profiles against b, we compared the model predictions with those determined from the observations. Since the observed kT of the halo is uniform within the data analyzed here, we fixed kT at 0.30 keV and retried all the spectral fitting to reduce uncertainty in the EM values. Figure 6 presents the thus-obtained EM values (shown as red circles) compared with the predictions from (i) the filled-halo model without bubbles (magenta) and (ii) a bubble-in-halo model assuming $R_{\rm in} = 3$ kpc, $R_{\rm out} = 5$ kpc, and $\theta = 10°$. Note that the vertical axis of Figure 6 is shown on a logarithmic scale and the corresponding EMs in the models were calculated from the same exact direction (l, b) coincident with each observation resulting in even larger fluctuations in the model line compared to that shown in Figure 5 (assuming $l = 0°$) owing to variations of l for each observational pointing (which were in the range $-20° < l < 20°$). A gas density at the halo center corresponding to model lines shown in Figure 6 is $n_0 = 0.13$ cm^{-3} for the filled-halo model without bubbles, and the gas density in the shell is $n_{\rm shell} = 3.4 \times 10^{-3}$ cm^{-3} for the bubble-in-halo model, which is doubled at low b wherever the northern and southern shells overlapped (Figure 3, top panel). Note that $n_{\rm shell}$ is almost consistent with what we observed for the NPS in Paper I, namely, $n_g \simeq 4 \times 10^{-3}$ cm^{-3}. Also, n_0 is consistent with that derived by Miller & Bregman (2013), $n_0 = 0.46^{+0.74}_{-0.35}$ cm^{-3}, within the stated errors.

Even with the simple picture and geometry assumed here, our models qualitatively explain the observed EM profiles against b, although it appears that the observations in the north bubble ($b > 0°$) favor the (ii) bubble-in-halo model, while those of the south bubble ($b < 0°$) favor the (i) filled-halo model without bubbles. Observationally, this corresponds to the fact that such a bright and giant X-ray structure like the NPS is

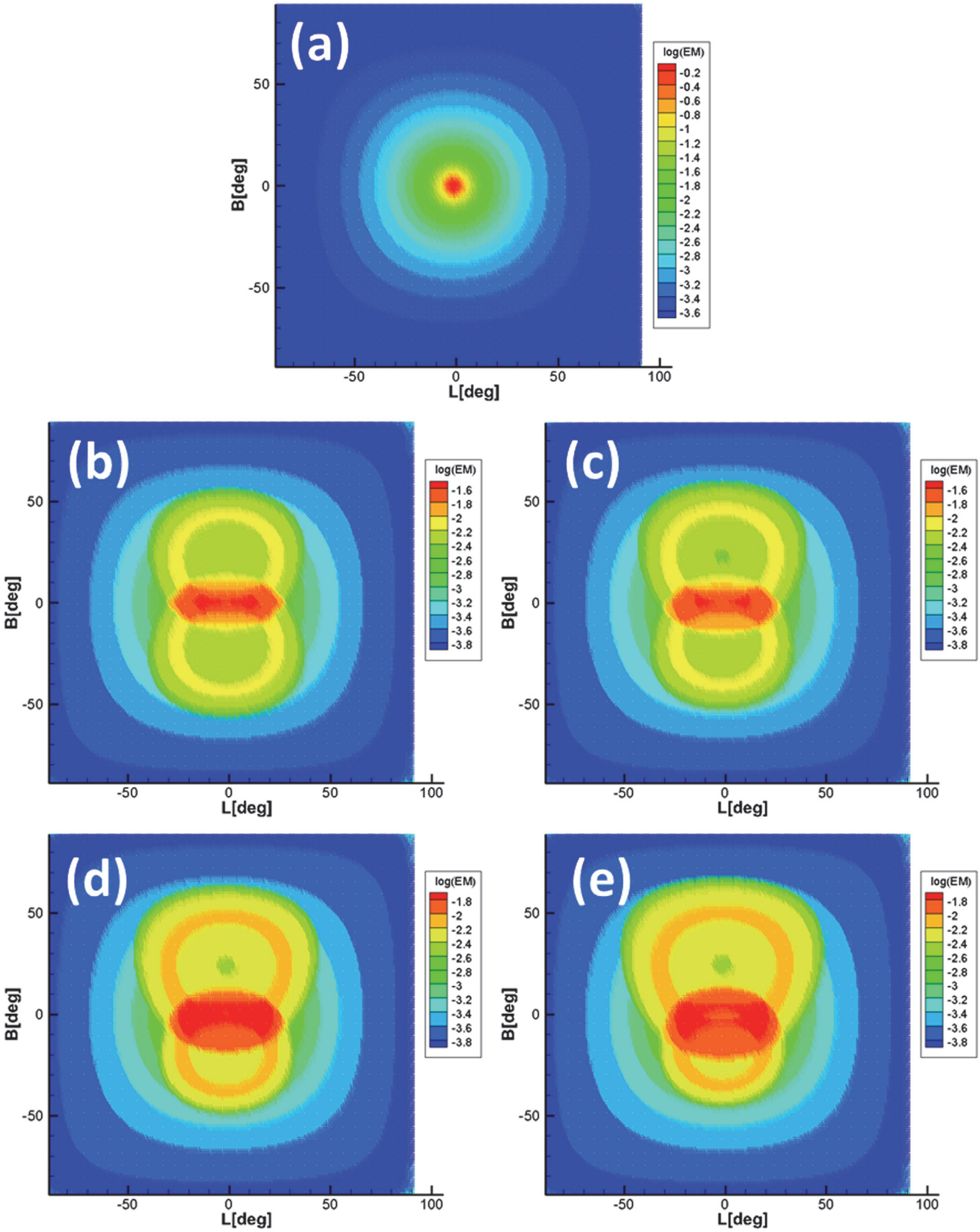

Figure 4. Variation of EM in the (l, b) plane as observed from the Sun in the (a) filled-halo model without bubbles, and bubble-in-halo models with (b) $\theta = 0°$, (c) $\theta = 10°$, (d) $\theta = 20°$, and (e) $\theta = 30°$.

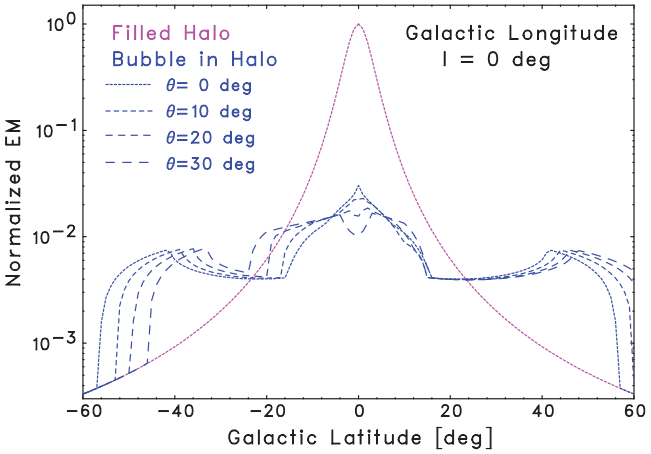

Figure 5. Variation of EM as a function of Galactic latitude b for (i) a filled-halo model without bubbles and (ii) bubble-in-halo models as measured with $l = 0°$. Different dashed lines correspond to inclination angles from $\theta = 0°$ to 30°.

unseen in the south, which is often taken as evidence supporting the idea that the NPS and the rest of the Loop I structure arises from a nearby supernova remnant (see detailed discussion in Paper I). However, if we look at the 408 MHz radio map (Haslam et al. 1982; Sofue 2000) closely, there is a southern counterpart of the NPS, the "South" Polar Spur (SPS) visible at $l \sim 20°$ extending from $(l, b) \sim (20°, 0°)$ toward (30°, −30°), although it is rather weak compared to the NPS (Sofue 2000). Also, a western counterpart of the SPS, which we call SPS-west, is found at $(l, b) \sim (340°, 0°)$ to (320°, −30°).

Interestingly, in our X-ray data, we can also see a similar excess feature in the south against the filled-halo model at $-50° < b < -30°$, which is relatively symmetric with respect to the NPS, but this excess is small compared to the NPS (see "SPS" in Figures 1 and 6). Here the ratio of observed EM to the filled-halo model is $\gtrsim 5$ for the NPS while only $\lesssim 2$ in the SPS. As shown in Figure 4, such a high degree of asymmetry in the north and south is difficult to explain solely by the inclination of bubbles' axis against the Galactic disk normal, thus suggesting an asymmetric outflow and/or initial density profile of the halo in which bubbles expand.

The asymmetry of the NPS and SPS with respect to the Galactic plane can be explained by both "local" and "bubble" models. Particularly as discussed in Paper I, the NPS and the rest of the Loop I structure may be nearby supernova remnants (SNRs) located at a distance of 170 pc. Such an asymmetry, however, can also be explained by a large-scale outflow from the GC and may not be exceptional in view of the fact that most shocked shells, such as SNRs and/or the GC phenomena, as well as extragalactic explosive events and bubbles, are more or less asymmetric like the NPS. An alternative model would be that the GH has a structural, as well as dynamical, asymmetry with respect to the Galactic plane and has an axis caused by an intergalactic wind (Sofue 1994, 2000). If the Galaxy is moving toward the northeast, e.g., $(l, b) \sim (130°, 30°)$, where the warping of the HI gas disk is the highest observed, the northern halo will suffer from a stronger northeast wind of typically $\sim 100\,\mathrm{km\,s^{-1}}$, while the southern halo is blocked from the wind by the Galactic disk. Such head/tail-winds to the bubbles and/or shocked shells could cause north–south (Galactic plane) as well as east–west (rotation axis) asymmetries in the sense that the northeast side is more enhanced, like in the NPS. Other more sophisticated modeling, including the intergalactic wind scenario, would be fruitful subjects for future simulations.

In this context, one may also consider how the asymmetry of the NPS and SPS with respect to the Galactic plane can be reconciled with the symmetric appearance of the gamma-ray bubbles observed with *Fermi*-LAT. If the former structures are physically associated with the bubbles, X-rays come from swept-up gas of the surrounding halo *outside* the bubbles that are clearly separated from the *inner* bubbles that emit gamma-rays. Thus, according to various external/initial conditions of halo gas into which the bubbles expand, the X-ray envelope can be far from being symmetric as seen in gamma rays. Moreover, by analogy with extragalactic radio lobes (e.g., Scheuer 1995, and discussion therein), the bubble angles to the line of sight are not individually constrained by the symmetric appearance of the bubbles in gamma rays (see also the case of the gamma-ray detection of the radio lobes of Cen A; Abdo et al. 2010). The lines of sight adopted in the cartoon modeling span ranges adopted for extragalactic radio galaxies whose lobes also appear symmetric.

Although the global structures, metallicity, and density profile of the halo in our Galaxy are still under investigation (e.g., Miller & Bregman 2013), future extensive studies using the MAXI-SSC (Matsuoka et al. 2009; Tsunemi et al. 2010) and *Astro-H* (Takahashi et al. 2014) will further clarify the origin, interaction, and dynamics between the hot gas halo and the bubbles. Particularly *Astro-H*, the sixth X-ray astronomy mission in Japan, carries the Soft X-ray Spectrometer (Mitsuda et al. 2014), which provides the capability for high-resolution X-ray spectroscopy with <7 eV (FWHM) in the energy range of 0.3–10 keV. In this context, Fox et al. (2015) reported two high-velocity metal absorption components centered at $v_{\rm LSR} = -235$ and $+250\,\mathrm{km\,s^{-1}}$ from ultraviolet spectra, which can be explained with an outflow velocity of $\gtrsim 900\,\mathrm{km\,s^{-1}}$ and a full opening angle of $\simeq 110°$. While the velocity is higher than in Papers I and II, such a value depends on the geometry of the biconical outflow assumed in the model. In this context, we note again that a slower velocity $v_{\rm exp} \sim 300\,\mathrm{km\,s^{-1}}$, which is consistent with Papers I and II, is implied by the X-ray absorption line toward 3C 273. Moreover, the presence of another $kT \simeq 0.7$ keV plasma, corresponding to $v_{\rm exp} \sim 600\,\mathrm{km\,s^{-1}}$, is reported in 2015. As discussed in detail in Inoue et al. (2015), precise measurements of metal abundances in the halo gas will provide crucial hints for the origin of the Fermi bubbles, either from the past activity of a GC-like AGN or from nuclear star-forming activity. As *Astro-H* will be launched in the winter of 2015, this will enable further progress toward clarifying the Fermi bubbles' nature.

5. CONCLUSION

In this paper we presented a systematic analysis of X-ray data provided by *Suzaku* (29 pointings) and *Swift* (68 pointings), covering sightlines through the entire spatial extent of the Fermi bubbles. We showed that (i) the temperature of the GH is surprisingly uniform with Galactic latitude with $kT \simeq 0.30 \pm 0.07$ keV; (ii) the EM, in contrast, varies widely by more than an order of magnitude, gradually decreasing toward high b; and (iii) the distribution of EM is asymmetric between the north and south bubbles. Although the association of the X-ray emission with the bubbles is not conclusive, we compared our observations with simple models assuming (i)

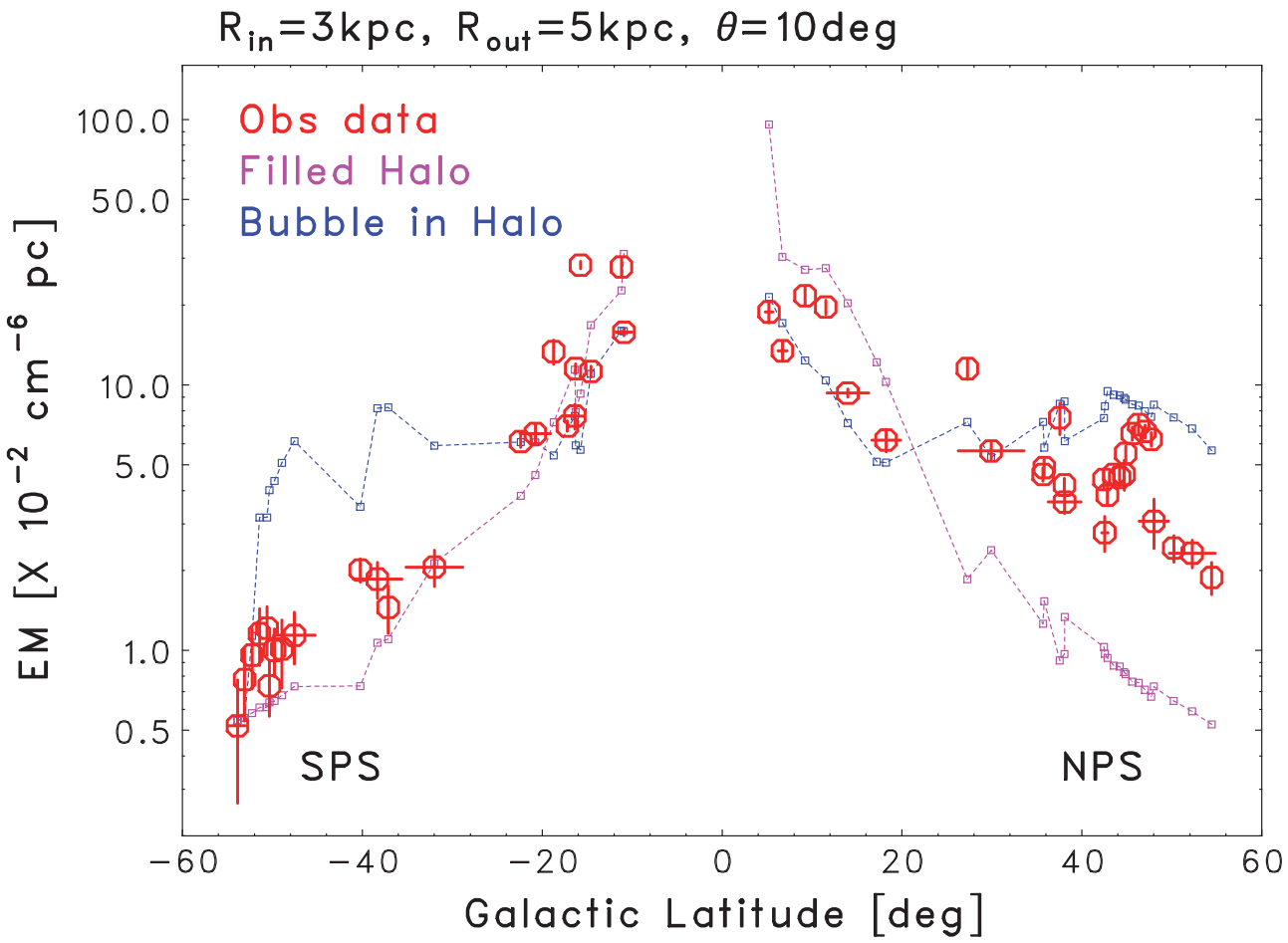

Figure 6. Variations in the observed spectral fitting parameters EM for the APEC2 emission component (red) as a function of Galactic latitude b, compared with a toy model as shown in Figures 3 and 4. A larger fluctuation in the model line than in Figure 4 is due to variations of l for each observational pointing, in the range $-20° < l < 20°$. Note that the profile from the "bubble-in-halo" model is consistent with the north bubble data, while the filled-halo model better represents the data for the south bubble (although note the clear excess corresponding to the SPS).

a filled halo without bubbles, whose gas density follows a hydrostatic isothermal β model; and (ii) a bubble-in-halo in which two identical bubbles expand within a halo forming a thick uniform shell of swept-up halo gas. We showed that a weak X-ray excess feature against the filled-halo model, the SPS, is evident in the south, but is rather weak compared to the NPS. Such a high degree of asymmetry is difficult to explain only by the effect of an inclined axis of the bubbles. This may suggest an asymmetric outflow and/or anisotropic initial density profile in situ, although this is inconclusive based on the current X-ray data presented in this paper.

We acknowledge the referee for useful suggestions that improved the manuscript. Work by C.C.C. at NRL is supported in part by NASA DPR S-15633 Y.

REFERENCES

Abdo, A. A., Ackermann, M., Ajello, M., et al. 2010, Sci, 328, 725
Ackermann, M., Albert, A., Atwood, W. B., et al. 2014, ApJ, 793, 64
Barthelmy, S. D., Barbier, L. M., Cummings, J. R., et al. 2005, SSRv, 120, 143
Bland-Hawthorn, J., & Cohen, M. 2003, ApJ, 582, 246
Burrows, D. N., Hill, J. E., Nousek, J. A., et al. 2005, SSRv, 120, 165
Carretti, E., Crocker, R. M., Staveley-Smith, L., et al. 2013, Natur, 493, 66
Cavaliere, A., & Fusco-Femiano, R. 1976, A&A, 49, 137
Crocker, R. M., & Aharonian, F. 2011, PhRvL, 106, 101102
Crocker, R. M., Bicknell, G. V., Carretti, E., Hill, A. S., & Sutherland, R. S. 2014, ApJL, 791, L20
Day, C., et al. 1998, The ASCA Data Reduction Guide, Tech. Rep. 355 (Greenbelt: NASA GSFC)
Dickey, J. M., & Lockman, F. J. 1990, ARA&A, 28, 215
Dobler, G., Finkbeiner, D. P., Cholis, I., Slatyer, T., & Weiner, N. 2010, ApJ, 717, 825
Fang, T., & Jiang, X. 2014, ApJL, 785, L24
Fox, A. J., Bordoloi, R., Savage, B. D., et al. 2015, ApJL, 799, L7
Fujimoto, R., Mitsuda, K., Mccammon, D., et al. 2007, PASJ, 59, 133
Fujita, Y., Ohira, Y., & Yamazaki, R. 2014, ApJ, 789, 67
Gehrels, N., Chincarini, G., Giommi, P., et al. 2004, ApJ, 611, 1005
Giommi, P., Angelini, L., Jacobs, P., & Tagliaferri, G. 1992, adass I, 25, 100
Guo, F., Mathews, W. G., Dobler, G., & Oh, S. P. 2012, ApJ, 756, 182
Haslam, C. G. T., Salter, C. J., Stoffel, H., & Wilson, W. E. 1982, A&AS, 47, 1
Henley, D. B., & Shelton, R. L. 2013, ApJ, 773, 92
Henley, D. B., Shelton, R. L., Kwak, K., Joung, M. R., & Mac Low, M.-M. 2010, ApJ, 723, 935
Hill, J. E., Burrows, D. N., Nousek, J. A., et al. 2004, Proc. SPIE, 5165, 217
Inoue, Y., Nakashima, S., Tahara, M., et al. 2015, PASJ, 67, 56
Ishisaki, Y., Maeda, Y., Fujimoto, R., et al. 2007, PASJ, 59, 113
Kataoka, J., Tahara, M., Totani, T., et al. 2013, ApJ, 779, 57
Kimura, M., Tsunemi, H., Tomida, H., et al. 2013, PASJ, 65, 14
King, I. 1962, AJ, 67, 471
Koyama, K., Maeda, Y., Sonobe, T., et al. 1996, PASJ, 48, 249
Koyama, K., Tsunemi, H., Dotani, T., et al. 2007a, PASJ, 59, 23
Koyama, K., Uchiyama, H., Hyodo, Y., et al. 2007b, PASJ, 59, 237
Kushino, A., Ishisaki, Y., Morita, U., et al. 2002, PASJ, 54, 327
Lacki, B. C. 2014, MNRAS, 444, L39
Matsuoka, M., Kawasaki, K., Ueno, S., et al. 2009, PASJ, 61, 999

Miller, M. J., & Bregman, J. N. 2013, ApJ, 770, 118
Mitsuda, K., Bautz, M., Inoue, H., et al. 2007, PASJ, 59, 1
Mitsuda, K., Kelley, R. L., Akamatsu, H., et al. 2014, Proc. SPIE, 9144, 91442A
Moretti, A., Gastaldello, F., Ettori, S., & Molendi, S. 2011, A&A, 528, A102
Moretti, A., Pagani, C., Cusumano, G., et al. 2009, A&A, 493, 501
Moretti, A., Vattakunnel, S., Tozzi, P., et al. 2012, A&A, 548, A87
Mou, G., Yuan, F., Bu, D., Sun, M., & Su, M. 2014, ApJ, 790, 109
Nakashima, S., Nobukawa, M., Uchida, H., et al. 2013, ApJ, 773, 20
Planck Collaboration, Ade, P. A. R., Aghanim, N., et al. 2013, A&A, 554, A139
Roming, P. W. A., Kennedy, T. E., Mason, K. O., et al. 2005, SSRv, 120, 95
Ryu, S. G., Nobukawa, M., Nakashima, S., et al. 2013, PASJ, 65, 33
Scheuer, P. A. G. 1995, MNRAS, 277, 331
Serlemitsos, P. J., Soong, Y., Chan, K.-W., et al. 2007, PASJ, 59, 9
Snowden, S. L., Freyberg, M. J., Plucinsky, P. P., et al. 1995, ApJ, 454, 643
Sofue, Y. 1977, A&A, 60, 327
Sofue, Y. 1984, PASJ, 36, 539
Sofue, Y. 1994, ApJL, 431, L91
Sofue, Y. 2000, ApJ, 540, 224
Su, M., Slatyer, T. R., & Finkbeiner, D. P. 2010, ApJ, 724, 1044
Tahara, M., Kataoka, J., Takeuchi, Y., et al. 2015, ApJ, 802, 91
Takahashi, T., Abe, K., Endo, M., et al. 2007, PASJ, 59, 35
Takahashi, T., Mitsuda, K., Kelley, R., et al. 2014, Proc. SPIE, 9144, 914425
Tawa, N., Hayashida, K., Nagai, M., et al. 2008, PASJ, 60, 11
Totani, T. 2006, PASJ, 58, 965
Tsunemi, H., Tomida, H., Katayama, H., et al. 2010, PASJ, 62, 1371
Weidenspointner, G., Skinner, G., Jean, P., et al. 2008, Natur, 451, 159
Yang, H.-Y. K., Ruszkowski, M., Ricker, P. M., Zweibel, E., & Lee, D. 2012, ApJ, 761, 185
Yao, Y., Nowak, M. A., Wang, Q. D., Shulz, N. S., & Canizares, C. R. 2008, ApJL, 672, L21
Yoshino, T., Mitsuda, K., Yamasaki, N. Y., et al. 2009, PASJ, 61, 805
Yuasa, T., Makishima, K., & Nakazawa, K. 2012, ApJ, 753, 129